







Photo-induced antiferromagnetic-ferromagnetic and spin-state transition in a double-perovskite cobalt oxide thin film

Yujun Zhang ^{1,2,3}✉, Tsukasa Katayama^{4,5,6}, Akira Chikamatsu ^{6,7}, Christian Schüßler-Langeheine ⁸, Niko Pontius⁸, Yasuyuki Hirata³, Kou Takubo³, Kohei Yamagami ³, Keisuke Ikeda³, Kohei Yamamoto ³, Tetsuya Hasegawa⁶ & Hiroki Wadati ^{2,3,9}

Investigation of ultrafast dynamic behaviors can provide novel insights about the coupling mechanisms among multiple degrees of freedom in condensed matters, such as lattice, magnetism and electronic structure. Here we investigate both the ferromagnetic (FM) and antiferromagnetic (AFM) dynamics of a strongly correlated oxide system, $\text{GdBaCo}_2\text{O}_{5.5}$ thin film by time-resolved x-ray magnetic circular dichroism in reflectivity (XMCDR) and resonant magnetic x-ray diffraction (RMXD). A photo-induced AFM-FM transition characterized by an increase of the transient XMCDR (sensitive to FM order) beyond the unpumped value and a decay of RMXD (sensitive to AFM order) was observed. The photon-energy dependence of the transient XMCDR and reflectivity could be interpreted as a concomitant photo-induced spin-state transition (SST). The AFM-FM transition and SST couple with each other in the time domain, resulting in unusual dynamic behaviors of the magnetism.

¹Institute of High Energy Physics, Chinese Academy of Sciences, Yuquan Road 19B, Shijingshan District, Beijing 100049, China. ²Graduate School of Materials Science, University of Hyogo, 3-2-1 Kouto, Kamigori-cho, Ako-gun, Hyogo 678-1297, Japan. ³Institute for Solid State Physics, University of Tokyo, 5-1-5 Kashiwanoha, Chiba 277-8581, Japan. ⁴Research Institute for Electronic Science, Hokkaido University, N20W10, Kita, Sapporo 001-0020, Japan. ⁵JST-PRESTO, Kawaguchi, Saitama 332-0012, Japan. ⁶Department of Chemistry, University of Tokyo, 7-3-1 Hongo, Bunkyo, Tokyo 113-0033, Japan. ⁷Department of Chemistry, Faculty of Science, Ochanomizu University, 2-1-1 Otsuka, Bunkyo-ku, Tokyo 112-8610, Japan. ⁸Helmholtz-Zentrum Berlin für Materialien und Energie GmbH, Albert-Einstein-Straße 15, 12489 Berlin, Germany. ⁹Institute of Laser Engineering, Osaka University, Suita, Osaka 565-0871, Japan. ✉email: zhangyujun@ihp.ac.cn

Ultrafast magnetic dynamics and transient magnetic states induced by optical excitation have attracted a lot of research interest^{1–10}. Pioneered by the observation of the ultrafast demagnetization in Ni metal¹, the magnetic dynamics of various material systems are intensely investigated to characterize the relevant timescales related to the magnetic degree of freedom. With the rapid development of synchrotron x-ray sources with pulsed time structures, the role of probe in pump-probe experiments can be played not only by optical lasers but also by synchrotron x-rays^{3–8} or x-ray free electron lasers^{9,10}. Synchrotron x-ray can provide multiple probing techniques with element specificity, such as x-ray magnetic circular dichroism (XMCD)^{3,4,9}, resonant magneto-optic Kerr effect¹⁰ and resonant x-ray scattering^{6–8}, etc. Capturing the element-specific dynamic behaviors of not only ferromagnetic (FM) order, but also anti-ferromagnetic (AFM) order and complex magnetic structures become possible by employing synchrotron-based resonant magnetic x-ray diffraction (RMXD)^{6–8}, which cannot be accessed by optical laser probes.

Materials with magnetic phase transitions are interesting from both views of fundamental science and practical application^{11–14}. Investigation of the magnetic dynamics can provide new perspectives to understand their magnetic phase transitions. One typical example is photo-induced AFM-FM transition observed in FeRh alloy¹⁴. FeRh exhibits an AFM-FM transition at ~ 370 K with increasing temperature¹³ and laser-pumping can promote AFM FeRh to a transient FM state¹⁴. However, due to the low photon energies of the magnetic sensitive Fe and Rh $L_{2,3}$ resonances, as well as the large Q -vector of the AFM order in FeRh¹³, it is technically unfeasible to directly investigate the dynamics of the AFM order even by using the synchrotron x-ray probes.

Recently, double perovskite $REBaCo_2O_x$ ($5 < x < 6$, RE : rare earth elements) systems^{15–18} have been continually studied due to their intriguing physical properties such as metal-insulator transition, AFM-FM transition, spin-state transition/ordering and high oxygen ionic conductivity, etc. As schematically shown in Fig. 1(a), due to the different ionic sizes of RE and Ba ions, A site of the perovskite lattice is often ordered into alternating RE and Ba layers. The oxygen concentration in these systems is often variable, leading to high oxygen mobility through the lattice¹⁸. When $x \approx 5.5$, the oxygen vacancies can order into columns along a -axis, resulting in non-equivalent Co sites coordinated by either oxygen octahedra or oxygen pyramids^{15–17,19,20}. The nominal valence state of Co is $3+$ and the competition between crystal field splitting and Hund coupling results in various spin-states such as low-spin (LS, $t_{2g}^6 e_g^0$, $S=0$), high-spin (HS, $t_{2g}^4 e_g^2$, $S=2$) and intermediate-spin (IS, $t_{2g}^5 e_g^1$, $S=1$) states^{15,16,19–24}. The spin-state of Co^{3+} is sensitive to temperature^{19–21}, pressure²², magnetic field²³, epitaxial strain²⁴ and lattice distortions^{15,16}, etc.

AFM-FM transitions coupled with spin-state transition (SST) was observed in some systems like $GdBaCo_2O_{5.5-x}$ ^{15,19}. Antiferromagnetism with an ordering vector of $(0\ 0\ 0.5)$ below ~ 230 K was detected in $GdBaCo_2O_{5.5-x}$ by RMXD thanks to its small AFM Q -vector¹⁵, providing the possibility to investigate the dynamics of both the FM and AFM orders simultaneously. A metal-insulator transition at ~ 350 K in $GdBaCo_2O_{5.5}$ (GBCO) was reported to be relevant to a SST at octahedral Co^{3+} sites^{19–21}, which is also promising to be triggered by laser excitation instead of elevated temperature. In this work we investigate the photo-induced FM and AFM dynamics of GBCO thin film by time-resolved (TR) XMCD in reflectivity (XMCDR) and TR-RMXD at Co L resonance within one experimental system. Photo-induced enhancement of XMCDR and decay of the RMXD were clearly observed, indicating a photo-induced AFM-FM transition. Photon energy dependence of the transient XMCDR and reflectivity

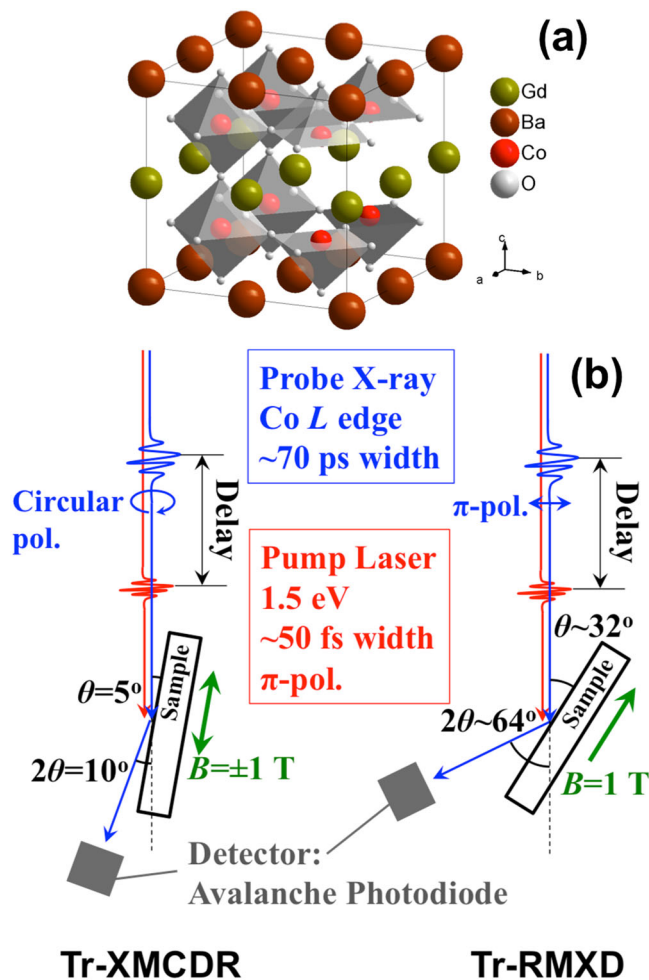


Fig. 1 Detection of antiferromagnetic/ferromagnetic dynamics of

GdBaCo₂O_{5.5} (GBCO). (a) Crystal structure of GBCO. Gd and Ba occupy the A site of the ABO_3 perovskite lattice, and Co occupies the B site of the ABO_3 perovskite lattice. (b) Setups of the time resolved x-ray magnetic circular dichroism in reflectivity and resonant magnetic x-ray diffraction experiments. B indicates the applied magnetic field during the measurement.

suggests a concomitant photo-induced SST. Both the electronic state change and the competition between AFM and FM exchange interactions simultaneously contribute to the observed magnetic dynamics.

Results and discussions

Characterization of the static properties. The 35-nm thick epitaxial GBCO thin film ($a=b=7.81\text{Å}$, $c=7.529\text{Å}$, the unit cell shown in Fig. 1(a)) was grown on $SrTiO_3(001)$ substrate by pulsed laser deposition and the detailed sample characterizations are reported elsewhere²⁵. Note that our GBCO film has finite magnetization in the AFM phase²⁵, which should be attributed to the competition between AFM and FM exchange interactions, either the canting of AFM moments¹⁵ or the coexistence of AFM and FM phases^{26,27}. The experimental setups of TR-XMCDR and TR-RMXD are schematically shown in Fig. 1(b) and explained in detail in the Methods part.

Figure 2 (a, b) show the static XMCDR of the GBCO thin film. Reflectivity R and XMCDR are defined as $R=(R_+ + R_-)/2$ and $\text{XMCDR}=(R_+ - R_-)/2$, respectively, where R_+ and R_- are the reflectivity measured by applying positive/negative magnetic

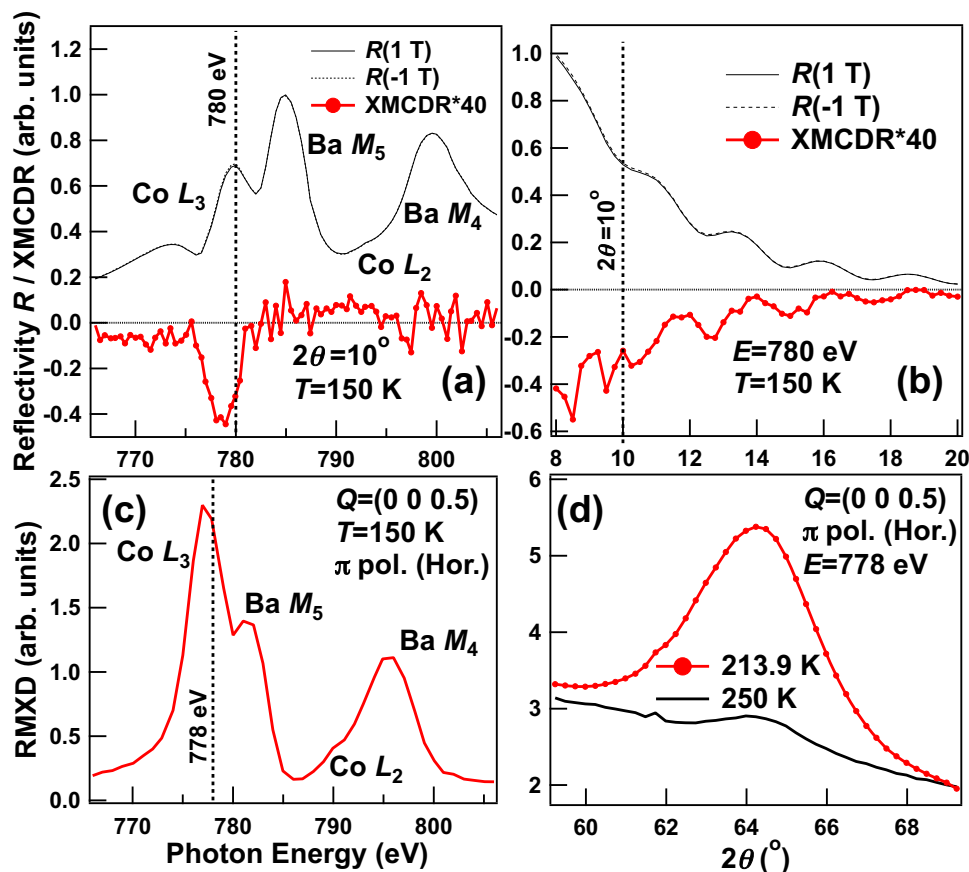


Fig. 2 Static x-ray magnetic circular dichroism in reflectivity (XMCDR) and resonant magnetic x-ray diffraction (RMXD). Photon energy scans (a) and θ - 2θ scans (b) of the static XMCDR and reflectivity with alternating magnetic field directions. Photon energy scan (c) and temperature-dependent θ - 2θ scans (d) of the static (0 0 0.5) RMXD. A constant magnetic field of 1 T was applied during the RMXD measurement.

fields. In the photon energy scans (Fig. 2(a)), it can be observed that Co L_3 resonance is located near Ba M_5 resonance and the XMCDR mainly appeared in the range from 775 eV to 782 eV, which represents the Co magnetization. The thickness fringes in θ - 2θ reflectivity curves at the Co L_3 resonance (Fig. 2(b)) are consistent with the nominal film thickness. An incident angle of $\theta=5^\circ$ was chosen as the optimum detection geometry for the following TR-XMCDR measurements. Static RMXD results of the AFM order are shown in Fig. 2(c, d). The photon energy scan (Fig. 2(c)) confirms the resonant behavior of the RMXD peak. The temperature-dependent θ - 2θ scans (Fig. 2(d)) confirm that the RMXD peak vanishes above 230 K and corresponds to the magnetic diffraction of the (0 0 0.5) AFM order, which is consistent with the previous report¹⁵. The correlation length of the AFM order was estimated as ~ 30.5 nm by the peak width²⁸ in Fig. 2(d), which is a little smaller than the film thickness possibly because of finite x-ray penetration depth or imperfections at the surface and interface. Photon energy was chosen at 778 eV for the TR-RMXD measurements.

Photo-induced AFM-FM transition. Since GBCO exhibits an AFM-FM transition with low-temperature AFM phase ($T_{\text{AFM-FM}} \sim 230$ K) and high-temperature FM phase ($T_C \sim 300$ K)^{15,19}, it can be expected that laser pumping can promote a transient FM state at temperatures below the AFM-FM transition, as observed in FeRh ($T_{\text{AFM-FM}} \sim 375$ K, $T_C \sim 680$ K)¹⁴. This prediction was confirmed by our TR-XMCDR measurements shown in Fig. 3(a). At 150 K, the transient increase of XMCDR beyond the unpumped value can be clearly observed. At lower laser fluences, the XMCDR increases

immediately after the laser illumination and reaches a maximum of $\sim 150\%$ of the unpumped XMCDR. At higher laser fluence of 12.32 mJ/cm², the XMCDR exhibits a fast decay followed by an increase of XMCDR beyond the unpumped value. Note that at 250 K (Fig. 3(b)), which is above the AFM-FM transition temperature, the increase of the XMCDR beyond the unpumped value was not observed, rather a normal fast demagnetization and a slow recovery appeared. This confirms the occurrence of a photo-induced AFM-FM transition in GBCO thin film. Interestingly, the reflectivity of the sample also exhibits significant decay-recovery behavior (Fig. 3(c, d)), inferring the concomitant change of electronic structure³. On the other hand, the TR-RMXD results in Fig. 3(e) indicate that the (0 0 0.5) AFM peak exhibits a normal decay-recovery process. Above the AFM-FM transition temperature (250 K, Fig. 3(f)), since the AFM peak does not exist anymore, no pump effect upon RMXD was observed. It can be clearly observed in Fig. 4 that laser-pumping mainly modifies the RMXD signal at the Co resonance, confirming that the decay of the antiferromagnetism is directly related to the Co sites.

As mentioned before, there is still finite net magnetization thus XMCDR signal in the AFM state of our GBCO film. On one hand, the AFM-FM transition could be understood as a continuous increase of the canting angle of Co moments in different AFM sublattices. At temperature below the magnetic transition, the Co moments are aligned antiferromagnetically with a canting angle to hold finite magnetization. The canting angle gradually change during the transition until the sublattice magnetization become parallel, which is featured by the disappearance of the AFM peak. In this picture the RMXD intensity represents the anti-parallel aligned component of the Co moments. On the other hand, a phase-separation picture can also fit in this explanation, in which

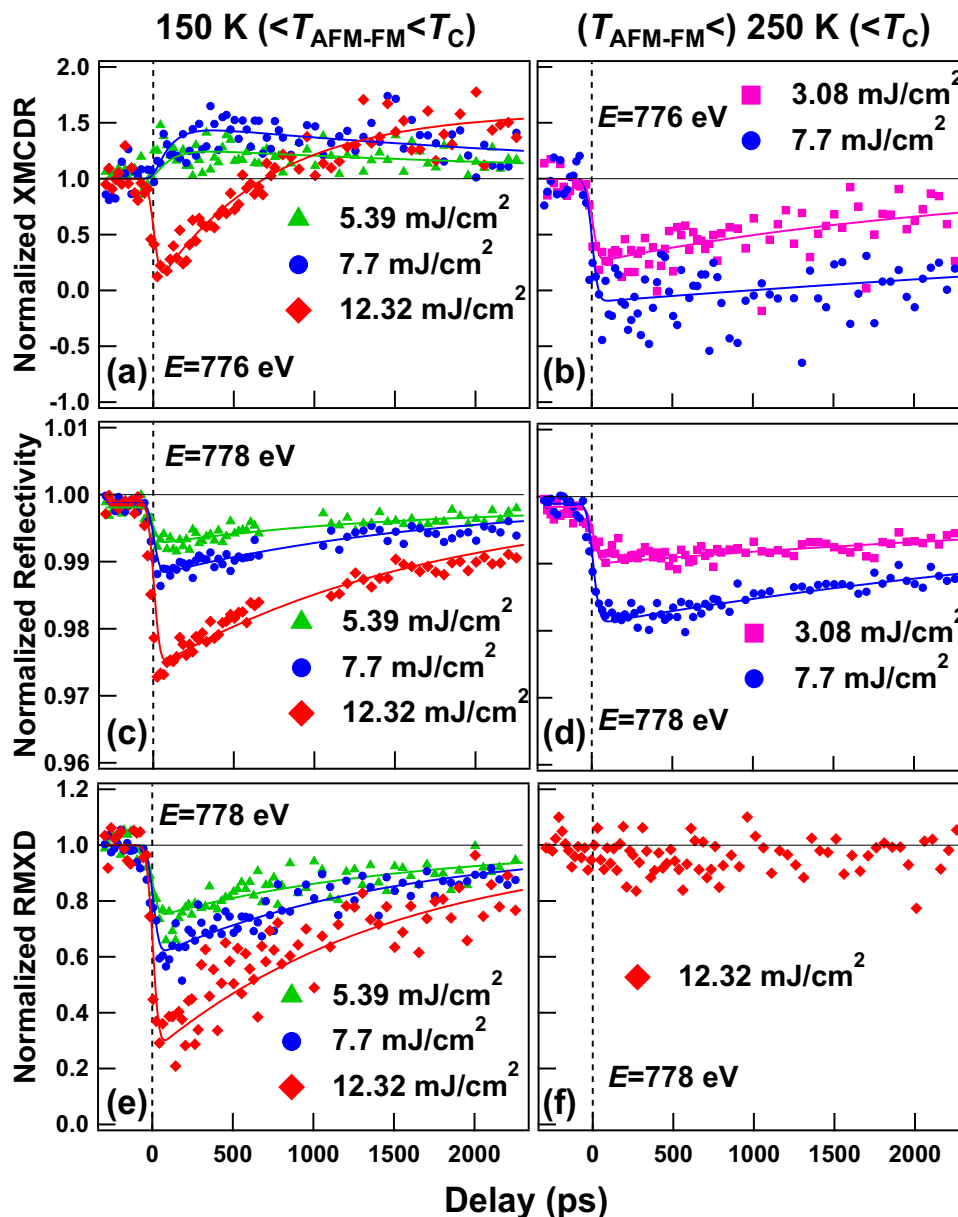


Fig. 3 Delay scans of time-resolved x-ray magnetic circular dichroism in reflectivity (XMCDR), reflectivity and resonant magnetic x-ray diffraction (RMXD). (a) TR-XMCDR at 150 K; (b) TR-XMCDR at 250 K; (c) TR-reflectivity at 150 K; (d) TR-reflectivity at 250 K; (e) TR-RMXD at 150 K; (f) TR-RMXD at 250 K. All signals shown are normalized to the unpumped values. The curves are fittings of the data by Eq. (1). Before normalizing to the unpumped value, the RMXD in (e) is processed by first subtracting the reflectivity background and then taking the square root so that the signal is proportional to the antiferromagnetic order parameter. The reflectivity background is calculated from the 250 K curve in Fig. 2(d), which should contain no RMXD signal. The RMXD in (f) is only normalized to the unpumped signal without subtracting the reflectivity background and taking square root. T_C and T_{AFM-FM} indicate the Curie temperature and the antiferromagnetic-ferromagnetic transition temperature, respectively.

both AFM and FM phases have collinearly aligned magnetic moments. Temperature or laser excitation only changes the relative ratio between these two competing phases. In this case the RMXD intensity represents the fraction of the collinear AFM phase. One should be able to distinguish these two pictures if the measurement has higher spatial resolution. But with the present spot size of x-ray, it is difficult to discriminate them. Nevertheless, the microscopic physical picture does not influence our following discussions and conclusions.

Thus, it can be understood from the results in Fig. 3 that when the laser fluence is low, photo-induced AFM-FM transition occurs with the increase of net magnetization characterized by XMCDR and the decrease of the anti-parallel aligned component

of Co moments characterized by the RMXD. When the laser fluence is as large as 12.32 mJ/cm², the fast decay of both XMCDR and RMXD could be attributed to a photo-induced demagnetization or other mechanisms, which will be discussed later. During the recovery process, GBCO first enters a more FM transient state and the XMCDR increases to a value above the unpumped value after ~1000 ps, as shown in Fig. 3(a).

The delay scans in Fig. 3 are fitted by a double-exponential function,

$$I(t) = I_1 \exp(-t/\tau_1) + I_2 [1 - \exp(-t/\tau_2)] \quad (1)$$

convolved with a 70-ps-wide Gaussian time-resolution function to estimate the timescales of the decay/enhancement and recovery

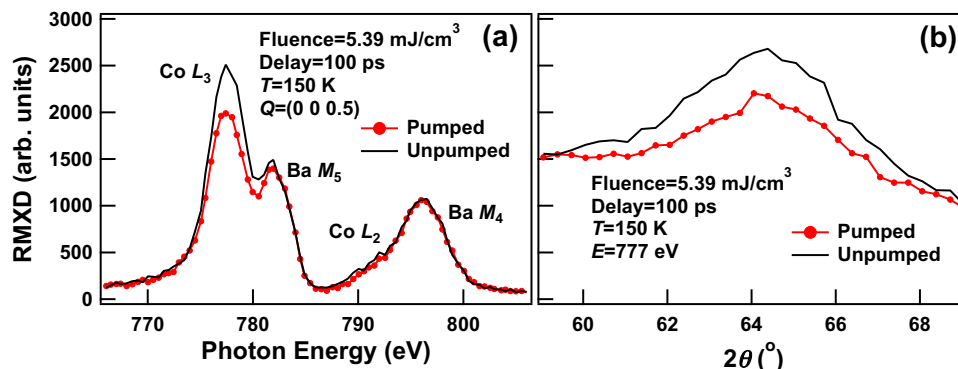


Fig. 4 Pump effects on energy and angular dependence of resonant magnetic x-ray diffraction (RMXD). Photon energy scan (a) and θ - 2θ scan (b) of the pumped/unpumped RMXD at $Q=(0\ 0\ 0.5)$. A constant magnetic field of 1 T was applied during the measurement.

Table 1 Fitted parameters of the dynamics of x-ray magnetic circular dichroism in reflectivity (XMCDR), reflectivity (R) and resonant magnetic x-ray diffraction (RMXD).

Temperature (K)	Measurement	Fluence (mJ/cm ²)	I_1	τ_1 (ps)	I_2	τ_2 (ps)
150	XMCDR	5.39	-0.280	101	0.281	3300
		7.7	-0.500	102	0.499	3300
		12.32	1.00	3.29	-1.60	700
	R	5.39	0.00548	3.12	-0.00545	1500
		7.7	0.0110	2.94	-0.0110	1700
		12.32	0.0250	2.92	-0.0250	1700
	RMXD	5.39	0.255	1.43	-0.254	1550
		7.7	0.400	4.96	-0.400	1500
		12.32	0.740	2.07	-0.740	1500
250	XMCDR	3.08	0.750	2.82	-0.750	2500
		7.7	1.10	2.28	-1.11	9950
		7.7	0.0180	8.44	-0.0185	4340
	R	3.08	0.0085	9.30	-0.00899	4380
		7.7	0.0180	8.44	-0.0185	4340
		7.7	0.0180	8.44	-0.0185	4340

I_1 , I_2 , τ_1 and τ_2 are parameters obtained by fitting the data in Fig. 3 by Eq. (1). I_1 and I_2 are the amplitude of the two dynamic components. τ_1 and τ_2 are the characteristic time of the two dynamic components.

processes. The fitted parameters are listed in Table 1. The decay processes are generally faster than the time resolution. The enhancement of XMCDR at fluences of 5.39 and 7.7 mJ/cm² occurs with a time constant of $\tau_1 \sim 100$ ps, which is significantly slower than the decay processes in other curves. The recovery processes of reflectivity and RMXD have similar timescales while the recovery of the XMCDR is significantly slower than that of the reflectivity and RMXD. This point will be explained in the following parts.

Possibility of photo-induced SST. To achieve a better understanding about the dynamic behaviors described above, we detailedly investigated the photon energy dependence of the transient XMCDR and reflectivity. Figure 5(a, b) show transient reflectivity and XMCDR spectra at a moderate laser fluence of 5.39 mJ/cm². At delay = 100 ps (Fig. 5(a)), the pump effect is strongly photon energy dependent. In the energy range from 775 eV to 778 eV, the absolute value of XMCDR is enhanced by the pump laser. While in the energy range from 778 eV to 782 eV, the pump laser does the opposite effect. In contrast, at delay=1400 ps (Fig. 5(b)), the absolute value of XMCDR is enhanced by the laser-pumping in the whole energy range of Co L_3 resonance. Laser-fluence dependence of the pump effect on the XMCDR (normalized to the corresponding unpumped values) can be more clearly observed in Fig. 5(c, d). When the laser fluence is small (green curves), a pump-induced spectral weight transfer of XMCDR from higher energy to lower energy can be observed at delay=100 ps (Fig. 5(c)) and then

the spectrum evolves into an overall positive pumping effect of XMCDR within the range of the Co L_3 resonance at delay=1400 ps (Fig. 5(d)). At higher laser fluences (blue and red curves), the increase of XMCDR is postponed by the decay process. The spectral weight transfer of XMCDR also infers a photo-induced electronic state transition. Delay-time-dependent transient reflectivity spectra shown in Fig. 5(e, f) can provide more insight. The pump effect of the reflectivity spectra is also strongly photon energy dependent. Laser-pumping causes an increase of reflectivity in the energy range from 776 eV to 777 eV and a decrease in the energy range near the resonance peak from 777 eV to 781 eV.

The spin-state of Co³⁺ in GBCO is still under debate. Previous reports state that the pyramidal Co ions are in either HS^{15,19} or IS^{20,21}. Octahedral Co³⁺ undergoes SST at ~ 350 K and various types of SSTs were proposed, such as LS-HS^{19,20} or IS-HS²¹. Nevertheless, one consensus is that pyramidal Co ions have stable spin-states and the octahedral Co ions are relevant to the SST¹⁹. Thus it is reasonable to predict that laser pumping can affect the spin-state of the octahedral Co³⁺. Here we adopt the ideas of stable HS at the pyramidal sites and a LS-HS transition at the octahedral sites for the following discussion.

Now we argue that a photo-induced LS-HS transition at the octahedral Co³⁺ sites, as also reported previously in LaCoO₃^{29,30}, likely occurs together with the AFM-FM transition. It is previously reported that in Co³⁺ perovskite oxides, when the population of HS octahedral Co³⁺ increases, the intensity at the peak of the Co L_3 resonance decreases and a smaller feature

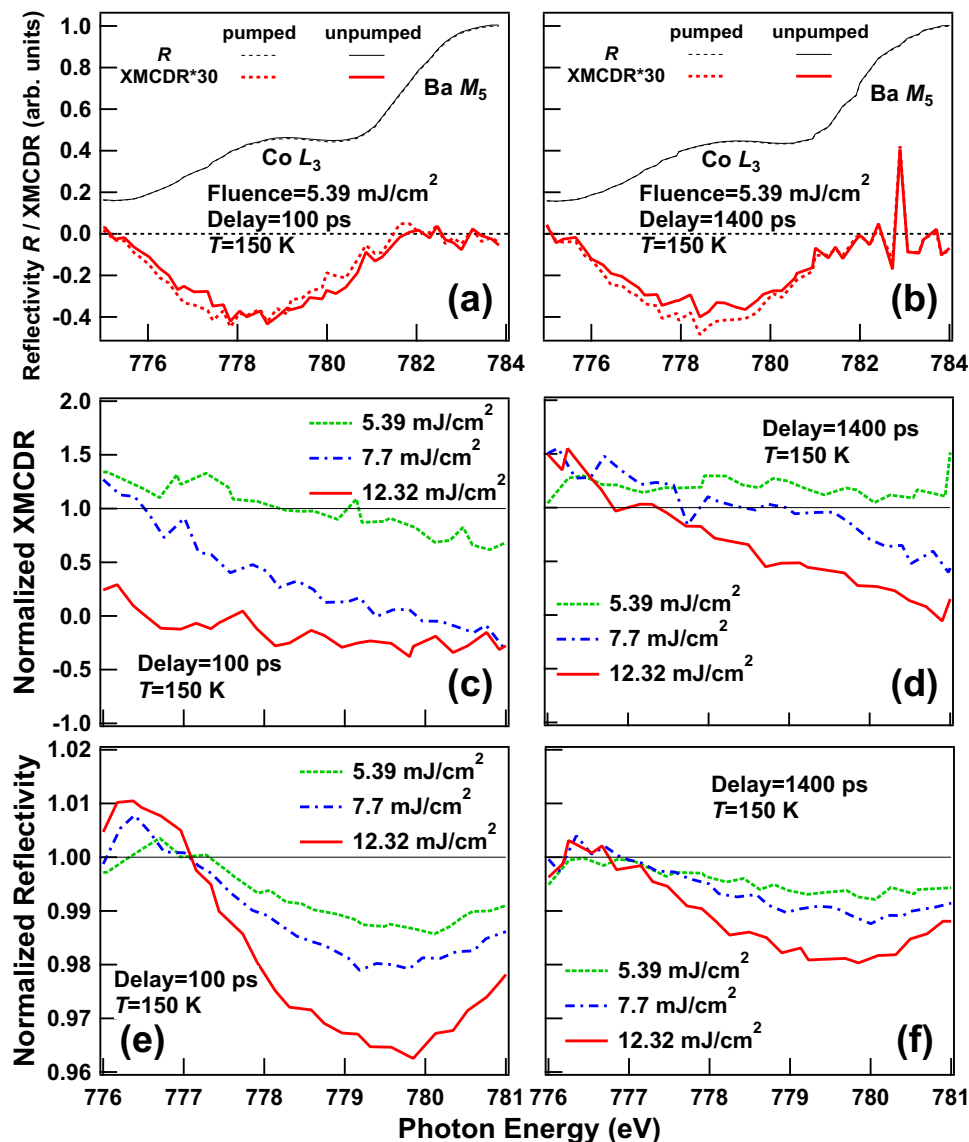


Fig. 5 Energy dependence of the pump effect on reflectivity and x-ray magnetic circular dichroism in reflectivity (XMCDR). Reflectivity and XMCDR spectra at ((a) Delay=100 ps; (b) Delay=1400 ps). Normalized XMCDR and reflectivity spectra at different delay time ((c) XMCDR, 100 ps; (d) XMCDR, 1400 ps; (e) Reflectivity, 100 ps; (f) Reflectivity, 1400 ps). Curves in (c–f) are normalized to the corresponding unpumped values.

increases at the lower energy side^{15,19}, which is consistent with the photo-induced change of transient reflectivity spectra reported here. At delay=100 ps, the similar direction of spectral weight transfer of XMCDR and reflectivity can be understood that HS Co³⁺ contributes more to the magnetization due to its larger magnetic moment. At delay=1400 ps, the XMCDR spectral weight shifts back to the unpumped position due to the recovery of spin-state at the octahedral sites. Another evidence of photo-induced electronic structure change is the inconsistent reaction speed of XMCDR and RMXD signals to the laser-pumping. If the pumping only changes the AFM canting angle or the AFM/FM ratio, the XMCDR should increase with the same speed as the RMXD decreases. Due to the finite energy-transfer efficiency between the electronic and the magnetic degrees of freedom, the slower increase of XMCDR is likely related to the change of AFM canting angle or the AFM/FM ratio, while the fast decay of RMXD seems to be dominated by the SST.

It is worth mentioning that photo-induced SST could not be predicated only by judging the spectral change of the reflectivity. There are other possible reasons for such spectral change, e.g.

valence change³¹ or charge disproportionation²⁹ of Co ions. But in GBCO we conclude that photo-induced SST is a most probable explanation for the observed spectral change. The photo-induced transitions in GBCO significantly differ from the temperature-triggered AFM-FM transitions and SSTs in similar perovskite cobaltates in the sense that transitions of both magnetism and electronic structure are involved simultaneously. Generally the AFM-FM transition and SST are separated by the difference of transition temperatures in cobaltates¹⁹.

Another question should be addressed when discussing the fast decay of RMXD signal. The decrease of RMXD at early delay times, such as delay < 100 ps, should be mainly attributed to the SST, rather than the change of AFM canting angle or the AFM/FM ratio. The LS-HS SST enhances the local moment, thus the decrease of RMXD could only be understood with further insight of the magnetic structure of GBCO. Due to the strong neutron absorption of Gd, neutron diffraction results and the exact magnetic structure of GBCO are barely reported. Thus here we refer to previously reported magnetic structures of other REBaCo₂O_x ($x \sim 5.5$, RE=Pr, Tb, etc.) systems^{16,32,33}, as

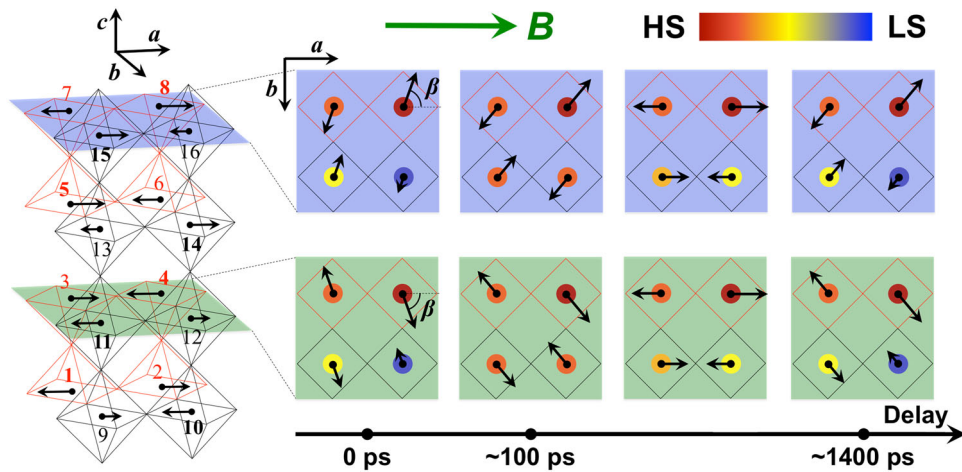


Fig. 6 Schematic of the photo-induced dynamics of magnetism and electronic structure of GdBaCo₂O_{5.5} in an antiferromagnetic sublattice moment canting picture. β denotes the antiferromagnetic sublattice canting angle. HS and LS indicate high-spin and low-spin states. B indicates the direction of the applied magnetic field. The red and black thin lines indicate the pyramidal and octahedral sites, respectively.

schematically shown in Fig. 6. Considering a full AFM unit cell of GBCO, there are 16 different Co sites (pyramidal sites 1-8 and octahedral sites 9-16). A full AFM unit cell consists of two magnetic sublattices (upper sublattice: sites 5-8 and 13-16; lower sublattice: sites 1-4 and 9-12). Here we assume that the moments align collinearly within each sublattice and lie in the a - b plane (parallel to the film surface)^{15,16}. In the picture of AFM sublattice canting, the AFM-FM transition can be described by the decrease of the canting angle β shown in Fig. 6. Note that additional structural modulation along a -axis^{15,34} makes the Co magnetic moment alternate along this direction, even though the adjacent Co ions have similar coordination environment. We also assume that the size of Co moments are identical for 4 groups of sites (group 1: sites 1,4,5,8; group 2: sites 2,3,6,7; group 3: sites 9,12,13,16; group 4: sites 10,11,14,15) in our following analysis. Here we calculate the change of RMXD and XMCDR signals during the continuous change of both the moment sizes at octahedral sites and the canting angle by using the following formula³⁵ (with the above-mentioned assumptions and π -polarized incident beam, only the π - σ channel contributes to the RMXD signal):

$$I_{\text{RMXD}} \propto \sum_{n=1}^{16} M_n \cos \psi_n \cos \theta e^{2\pi i \vec{Q} \cdot \vec{r}_n}; \quad I_{\text{XMCDR}} \propto \sum_{n=1}^{16} M_n \sin \psi_n \quad (2)$$

where M_n is the moment size of the n th site, ψ_n is the clockwise angle from $-b$ axis to the moment direction when looking along the $-c$ direction (for the upper sublattice $\psi_n = \pm(\pi/2 - \beta)$, for the lower sublattice $\psi_n = \pm(\pi/2 + \beta)$), $\theta = 32^\circ$ is the scattering angle, $Q = (0 \ 0 \ 0.5)$, and \vec{r}_n is the atom coordinate of the n th site in the unit cell shown in Fig. 6. To reproduce the decrease of RMXD induced by SST at the octahedral sites, a larger increase of $M_{9,12,13,16}$ than $M_{10,11,14,15}$ is necessary. The laser pumping effects upon XMCDR due to the β -decrease and the M_n -increase compete with each other. We demonstrate in Fig. 7(a) that with certain change of M_n and β , it is possible to qualitatively reproduce the fluence scans of XMCDR and RMXD at delay=100 ps (Fig. 7(b)). The fast decay of XMCDR at high laser fluence (Fig. 3(a), 12.32 mJ/cm²) is also reproduced in the calculation, which may not only originate from the photo-induced demagnetization mentioned before. Note that although the calculation is conducted with the scattering plane of a - c plane and magnetic field parallel to a , the result will be the same if the scattering plane is the b - c plane and magnetic field is along b .

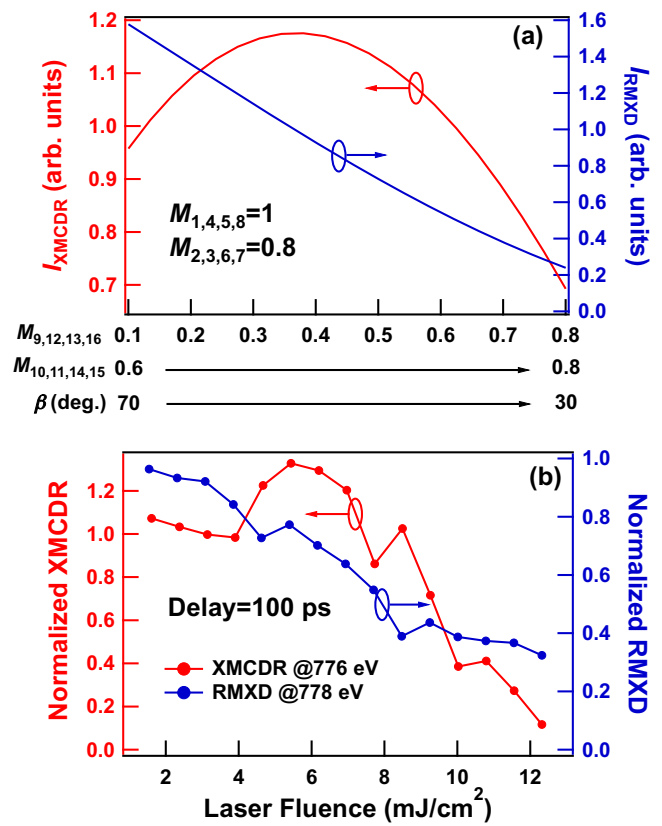


Fig. 7 Laser-pumping effect upon x-ray magnetic circular dichroism in reflectivity (XMCDR) and resonant magnetic x-ray diffraction (RMXD) signals. (a) XMCDR and RMXD calculated by Eq. (2) with assumption of certain change of spin-state (represented by the moment sizes M_n) and AFM sublattice canting angle β . (b) Laser fluence dependence of the XMCDR and RMXD signals at delay=100 ps measured at 150 K.

These two scattering configurations should be equivalently populated due to the in-plane 4-fold symmetry of the SrTiO₃(001) substrate. Although the discussions above are based on the picture of sublattice moment canting, they can also fit in the phase separation picture when the factor $\cos\beta$ is replaced by the AFM/FM ratio.

Now we can comprehensively describe the photo-induced dynamic behaviors of GBCO, as schematically shown in Fig. 6. Laser illumination significantly changes the electronic structure of GBCO thin film, which can be characterized by the reflectivity. At the same time, pump laser also induces an AFM-FM transition, which is featured by the increase of XMCDR and decrease of the RMXD. The processes related to the magnetic degree of freedom can be interpreted as the change of either the AFM canting angle or the AFM/FM ratio. In Fig. 6 we are using the picture of AFM sublattice moment canting and the discussion should be analogous in the picture of phase separation. The system is first pumped into a FM state with more fraction of HS octahedral Co^{3+} . The enhancement of XMCDR should be attributed to both the more parallel alignment of Co moments and the change of individual Co^{3+} moment size due to the SST. Then the magnetism and spin-state relax with comparable speed. When a simple double exponential fitting is applied, the contribution from both origins makes the fitted recovery timescale of XMCDR much slower than the recovery timescales of either reflectivity or RMXD. Meanwhile, the noise level of the XMCDR data cannot support meaningful fittings with more than two exponential functions. At high laser fluences, the fast decay of XMCDR may be attributed to both the decrease of canting angle and demagnetization. Afterwards the system enters a transient state with higher net magnetization than the unpumped state, before further recovering to the original AFM state with mainly LS state at octahedral Co^{3+} sites.

Conclusions

To conclude, in this work we investigated the dynamics of both FM and AFM orders as well as the electronic structure in GBCO thin film by time-resolved synchrotron resonant x-ray scattering techniques. A photo-induced AFM-FM transition coupled with SST at octahedral Co^{3+} sites was confirmed by comprehensive investigations of laser-fluence, delay-time, and photon-energy dependencies of the dynamic behaviors. The simultaneous contribution of moment alignment and spin-state change to the magnetism in the transient state gives rise to the dynamic behaviors of XMCDR, reflectivity and RMXD. The measured laser-pumping effect is qualitatively consistent with calculation results by considering the detailed magnetic structure of GBCO. Our investigation presents a photo-induced AFM-FM transition in a strongly correlated oxide system and a new category of photo-induced phenomena involving both magnetic and electronic-structure degrees of freedom. The results indicate significant coupling of magnetism and electronic structure in strongly correlated systems, not only in static states but also in transient states and dynamic behaviors.

Methods

The TR-XMCDR and TR-RMXD measurements were performed at beamline UE56/1-ZPM (FEMTOSPEX) of BESSY II by using the setups shown in Fig. 1(b). For TR-XMCDR measurements, x-ray with fixed circular polarization at the Co L edge was used and an in-plane magnetic field of ± 1 T was switched to observe the magnetic contrast of the reflectivity. The incident angle was fixed at 5° . The reflectivity was detected with an avalanche photodiode and boxcar integrated. For TR-RMXD measurements, we used horizontal linearly polarized x-ray (π -polarization) instead to enhance the magnetic diffraction, with a constant in-plane magnetic field of 1 T applied. The diffraction signal was integrated via photon counting. A Ti:sapphire laser ($\lambda=800$ nm, π -polarization, 3 kHz, pulse width ~ 50 fs) was employed as the pump source. The full width at half maximum (FWHM) spot sizes (horizontal \times vertical) of the pump laser and the probe x-ray were around 0.34×0.38 mm² and 0.12×0.04 mm², respectively. The time resolution of the measurements was limited to ~ 70 ps by the pulse width of the probe x-ray. The pumped and unpumped signals were collected alternatively by recording the contributions from the pumped and unpumped bunches. The sample temperature was controlled by a liquid N_2 flow cryostat. Since the measurement geometries of XMCDR and RMXD were different, the surface-transmitted laser fluence was calibrated by measuring the incident-angle dependence of the laser power reflected by the sample surface. All the laser fluences mentioned below are calibrated fluences which are absorbed by the sample.

Data availability

The data that support the findings of this study are available from the corresponding author upon reasonable request.

Received: 17 September 2021; Accepted: 7 February 2022;

Published online: 07 March 2022

References

1. Beaurepaire, E., Merle, J. C., Daunois, A. & Bigot, J. Y. Ultrafast spin dynamics in ferromagnetic nickel. *Phys. Rev. Lett.* **76**, 4250 (1996).
2. Ogasawara, T. et al. General features of photoinduced spin dynamics in ferromagnetic and ferrimagnetic compounds. *Phys. Rev. Lett.* **94**, 087202 (2005).
3. Tsuyama, T. et al. Photoinduced demagnetization and insulator-to-metal transition in ferromagnetic insulating BaFeO_3 thin films. *Phys. Rev. Lett.* **116**, 256402 (2016).
4. Takubo, K. et al. Capturing ultrafast magnetic dynamics by time-resolved soft x-ray magnetic circular dichroism. *Appl. Phys. Lett.* **110**, 162401 (2017).
5. Kirilyuk, A., Kimel, A. V. & Rasing, T. Ultrafast optical manipulation of magnetic order. *Rev. Mod. Phys.* **82**, 2731 (2010).
6. Pontius, N. et al. Time-resolved resonant soft x-ray diffraction with free-electron lasers: Femtosecond dynamics across the Verwey transition in magnetite. *Appl. Phys. Lett.* **98**, 182504 (2011).
7. Chuang, Y. D. et al. Real-Time manifestation of strongly coupled spin and charge order parameters in stripe-ordered $\text{La}_{1.75}\text{Sr}_{0.25}\text{NiO}_4$ nickelate crystals using time-resolved resonant x-ray diffraction. *Phys. Rev. Lett.* **110**, 127404 (2013).
8. Dean, M. P. M. et al. Ultrafast energy- and momentum-resolved dynamics of magnetic correlations in the photo-doped Mott insulator Sr_2IrO_4 . *Nat. Mater.* **15**, 601 (2016).
9. Yamamoto, K. et al. Ultrafast demagnetization of Pt magnetic moment in L10-FePt probed by magnetic circular dichroism at a hard x-ray free electron laser. *N. J. Phys.* **21**, 123010 (2019).
10. Yamamoto, K. et al. Element-selectively tracking ultrafast demagnetization process in Co/Pt multilayer thin films by the resonant magneto-optical Kerr effect. *Appl. Phys. Lett.* **116**, 172406 (2020).
11. Salamon, M. B. & Jaime, M. The physics of manganites: Structure and transport. *Rev. Mod. Phys.* **73**, 583 (2001).
12. Ward, T. Z. et al. Elastically driven anisotropic percolation in electronic phase-separated manganites. *Nat. Phys.* **5**, 885 (2009).
13. Moruzzi, V. L. & Marcus, P. M. Antiferromagnetic-ferromagnetic transition in FeRh. *Phys. Rev. B* **46**, 2864 (1992).
14. Radu, I. et al. Laser-induced generation and quenching of magnetization on FeRh studied with time-resolved x-ray magnetic circular dichroism. *Phys. Rev. B* **81**, 104415 (2010).
15. García-Fernández, M. et al. Magnetic and electronic Co states in the layered cobaltate $\text{GdBaCo}_2\text{O}_{5.5-x}$. *Phys. Rev. B* **78**, 054424 (2008).
16. Miao, P. et al. Hole-doping-induced melting of spin-state ordering in $\text{PrBaCo}_2\text{O}_{5.5+x}$. *Phys. Rev. B* **95**, 125123 (2017).
17. Katayama, T. et al. Ferromagnetism with strong magnetocrystalline anisotropy in A-site ordered perovskite YBaCo_2O_6 epitaxial thin films prepared via wet-chemical topotactic oxidation. *J. Mater. Chem. C* **6**, 3445 (2018).
18. Taskin, A. A., Lavrov, A. N. & Ando, Y. Achieving fast oxygen diffusion in perovskites by cation ordering. *Appl. Phys. Lett.* **86**, 091910 (2015).
19. Hu, Z. et al. Spin-state order/disorder and metal-insulator transition in $\text{GdBaCo}_2\text{O}_{5.5}$: Experimental determination of the underlying electronic structure. *N. J. Phys.* **14**, 123025 (2012).
20. Frontera, C., García-Muñoz, J. L., Llobet, A. & Aranda, M. A. G. Selective spin-state switch and metal-insulator transition in $\text{GdBaCo}_2\text{O}_{5.5}$. *Phys. Rev. B* **65**, 180405(R) (2002).
21. Roy, S., Khan, M., Guo, Y. Q., Craig, J. & Ali, N. Observation of low, intermediate, and high spin states in $\text{GdBaCo}_2\text{O}_{5.45}$. *Phys. Rev. B* **65**, 064437 (2002).
22. Vogt, T., Hriljac, J. A., Hyatt, N. C. & Woodward, P. Pressure-induced intermediate-to-low spin state transition in LaCoO_3 . *Phys. Rev. B* **67**, 140401(R) (2003).
23. Kimura, S. et al. Field-induced spin-state transition in the perovskite cobalt oxide $\text{Sr}_{1-x}\text{Y}_x\text{CoO}_{3-\delta}$. *Phys. Rev. B* **78**, 180403(R) (2008).
24. Yokoyama, Y. et al. Tensile-strain-dependent spin states in epitaxial LaCoO_3 thin films. *Phys. Rev. Lett.* **120**, 206402 (2018).
25. Katayama, T. et al. Ionic order engineering in double-perovskite cobaltite. *Chem. Mater.* **33**, 5675–5680 (2021).
26. Wu, J. & Leighton, C. Glassy ferromagnetism and magnetic phase separation in $\text{La}_{1-x}\text{Sr}_x\text{CoO}_3$. *Phys. Rev. B* **67**, 174408 (2003).
27. Hoch, M. J. R. et al. Evolution of the ferromagnetic and nonferromagnetic phases with temperature in phase-separated $\text{La}_{1-x}\text{Sr}_x\text{CoO}_3$ by high-field ^{137}La NMR. *Phys. Rev. B* **70**, 174443 (2004).

28. Yamamoto, K. et al. Thickness dependence and dimensionality effects on charge and magnetic orderings in $\text{La}_{1/3}\text{Sr}_{2/3}\text{FeO}_3$ thin films. *Phys. Rev. B* **97**, 075134 (2018).
29. Izquierdo, M. et al. Laser-induced charge-disproportionated metallic state in LaCoO_3 . *Phys. Rev. B* **90**, 235128 (2014).
30. Izquierdo, M. et al. Monitoring ultrafast metallization in LaCoO_3 with femtosecond soft x-ray spectroscopy. *Comm. Phys.* **2**, 8 (2019).
31. Guillou, F. et al. Coupled valence and spin state transition in $(\text{Pr}_{0.7}\text{Sm}_{0.3})_{0.7}\text{Ca}_{0.3}\text{CoO}_3$. *Phys. Rev. B* **87**, 115114 (2013).
32. Plakhty, V. P. et al. Spin structure and magnetic phase transitions in $\text{TbBaCo}_2\text{O}_{5.5}$. *Phys. Rev. B* **71**, 214407 (2005).
33. Khalyavin, D. D. Magnetic ground state of $\text{LBaCo}_2\text{O}_{5.5/5.44}$ cobalt oxides. *Phys. Rev. B* **72**, 134408 (2005).
34. Chernenkov, Y. P. et al. X-ray diffraction study of superstructure in $\text{GdBaCo}_2\text{O}_{5.5}$. *Phys. Rev. B* **71**, 184105 (2005).
35. Fink, J., Schierle, E., Weschke, E. & Geck, J. Resonant elastic soft x-ray scattering. *Rep. Prog. Phys.* **76**, 056502 (2013).

Acknowledgements

Y. Z. thanks the supports from Natural Science Foundation of China (Grant No. 52002370) and Basic Research Funding of IHEP (Grant No. Y9515560U1). This work was supported by MEXT Quantum Leap Flagship Program (MEXT Q-LEAP) Grant No. JPMXS0118068681 and JSPS KAKENHI Grant No. 19H01816, 19H05824, 19H02594 and 17F17327. We thank HZB for the allocation of synchrotron radiation beamtime (Proposals 201-09271ST, 191-07992ST and 192-08474ST/R), Karsten Holldack and Rolf Mitzner for experimental support, and the supports provided by Nippon Sheet Glass Foundation for Materials Science and Engineering.

Author contributions

H.W. and T.H. supervised the research and conceived the experiments. T.K. and A.C. prepared the GBCO film. Y.Z., C.S.-L., N.P., Y.H., K.T., K. Yamagami, K.I. and K. Yamamoto conducted the time-resolved synchrotron experiments. Y.Z. prepared the manuscript. All the authors contributed to the analysis of the results.

Competing interests

The authors declare no competing interests.

Additional information

Supplementary information The online version contains supplementary material available at <https://doi.org/10.1038/s42005-022-00823-4>.

Correspondence and requests for materials should be addressed to Yujun Zhang.

Peer review information *Communications Physics* thanks Sergei Naumov and the other, anonymous, reviewer(s) for their contribution to the peer review of this work. Peer reviewer reports are available.

Reprints and permission information is available at <http://www.nature.com/reprints>

Publisher's note Springer Nature remains neutral with regard to jurisdictional claims in published maps and institutional affiliations.



Open Access This article is licensed under a Creative Commons Attribution 4.0 International License, which permits use, sharing, adaptation, distribution and reproduction in any medium or format, as long as you give appropriate credit to the original author(s) and the source, provide a link to the Creative Commons license, and indicate if changes were made. The images or other third party material in this article are included in the article's Creative Commons license, unless indicated otherwise in a credit line to the material. If material is not included in the article's Creative Commons license and your intended use is not permitted by statutory regulation or exceeds the permitted use, you will need to obtain permission directly from the copyright holder. To view a copy of this license, visit <http://creativecommons.org/licenses/by/4.0/>.

© The Author(s) 2022